Design and Numerical Analysis of A 3 kWe Flameless MicroTurbine Combustor for Hydrogen Fuel

Bahamin Bazooyar[1]

Hamidreza Gohari Darabkhani[2,*]

Department of Design & Engineering, School of Creative Arts and Engineering, Staffordshire University, Stoke-on-Trent, ST4 2DE, United Kingdom

[1]Bahamin Bazooyar, Research Fellow in Turbulent Combustion (b.bazooyar@staffs.ac.uk)

[2,*]Corresponding author: Hamidreza Gohari Darabkhani, Professor of Low Carbon and Renewable Energy Systems

Email: h.g.darabkhani@staffs.ac.uk , h.g.darabkhani@gmail.com

Tel: +44 (0) 1782 292769

ABSTRACT: In this work, a new 3 kWe flameless combustor for hydrogen fuel is designed and analyzed using CFD simulation. The strategy of the design is to provide a large volumetric combustion for hydrogen fuel without significant rise of the temperature. The combustor initial dimensions and specification were obtained from practical design procedures initially, and then optimized from CFD simulations. To this end, a three-dimensional model for the designed combustor is constructed to further analysis of flameless hydrogen combustion and consideration that leads to disappearance of flame-front and flameless combustion. The key design parameters including aerodynamic, temperature at walls and flame, NO_X, pressure drop, combustion efficiency for the hydrogen flame is analyzed in the designed combustor. To well demonstrate the combustor, the NO_X and entropy destruction and finally energy conversion efficiency, and overall operability in the microturbine cycle of hydrogen flameless combustor is compared with a 3 kWe design counterpart for natural gas. The findings demonstrate that hydrogen flameless combustion is superior to derive the microturbines with significantly lower NO_X, and improvements in energy efficiency, and cycle overall efficiency with low wall temperatures guaranteeing the long-term operation of combustor and microturbine parts.

Keywords: Hydrogen, microturbine, flameless combustor, low NO_X, low carbon.

1. Introduction

The hydrogen is one of the most promising future fuels as it could be derived from both renewable and nonrenewable energy sources [1]. While it is the most abundant element in cosmos, it cannot be usually found pure on earth because it is light and escape from the earth atmosphere [2]. The production of hydrogen at large scales currently faces many economical and operational challenges. These challenges include explosive hazards, high adiabatic flame temperature, significant NO_X emission, and current unavailable reliable source [3, 4]. In small scales, in contrast, the hydrogen can be currently produced from the electrolysis or methane reforming [5], both promising the application

of hydrogen as a potential fuel in micropower generators. In addition, many of the challenges of hydrogen as a fuel can be easily overcome by implementing it as a fuel in small energy gensets.

The small power generators efficient are energy genets because the rate of energy loss from their compact parts is minimum. In order to improve the energy conversion efficiency of these devices further, the main attention should be given to their combustor. The combustor determines the outlet temperature uniformity, the power efficiency, and the level of pollutant [6, 7]. Along with a successful design of the combustor, the application of a renewable high calorific fuel could benefit the micropower generator by simultaneously increasing the effectiveness and decreasing the pollutions [8-15]. Hydrogen is a good candidate for this purpose as it has three times the energy density per weight as methane or gasoline while does carry no carbon emissions (CO, CO_2, VOC, and PAH). Because of these specific characteristics, the adiabatic flame of hydrogen flame is high which create the potential for significant thermal NO [16, 17]. This make it necessary to come up with strategies to control the temperature. The application of hydrogen could be considered as either an additive to other conventional fuels or if it is diluted by an inert gas. One significant strategy is to use hydrogen with nitrogen which lead to a high volumetric flameless combustion under the controlled temperature-so called autoignition. However, the rate of mixing in the combustor should be carefully managed to hamper any strong agitation of hydrogen with oxygen, and as a result significant NO_X formation. This could be achieved in a carefully designed combustor with ignition occurring via diffusion of hydrogen and nitrogen rather than turbulent mixing. The autoignition of H_2/N_2 flame in terms of flame stabilization, autoignition, flame and turbulence structure, swirl dynamic, extinction and ignition [18-26] has been thoroughly researched using experimental and numerous numerical methods in a non-premixed imitated environment. However, it was rarely utilized and analyzed in micropower generators for production of power and energy. The UK government also aspires to decarbonizing, or reducing the carbon content of the UK gas supply that is one the option for reducing the emissions from heat and power generation. In this work, a 3 KWe microturbine power generator with a recuperated combustor is chosen as a case study. First, the

application of H_2/N_2 was verified in terms of the required amount of fuel and the optimum proportion of hydrogen to nitrogen to obtain the desired power. Second, the renewable combustor designed by is analyzed in the microturbine in terms of emission, energy, and exergy. Thirdly, the addition of hydrogen is analyzed as an additive to methane in the designed microturbine combustor.

2. Combustor design

The primary objective was to design a microturbine combustor that could drive a 3 kWe turbine. Other combustor parametric design outlooks include 47 kW heat output power, 3% overall pressure drop, 0.05 kg/s recuperated air mass flow rate at 850 K and 180 kPa, and 1100 K combustor outlet temperature. A vortex combustor to provide the following operational conditions is designed and optimized using the CFD calculation. The dimensions of the combustor was obtained from the Lefebvre practical formulation [27]. Fig 1 shows the schematic of the combustor. The diameters of the combustor liner and casing are 46 and 58 mm. The length of the liner and combustor nozzle are 135 and 264 mm. A 10 cm long entrance duct for the combustor is considered which is connected to a conic wall angled 60^o from axis of the combustor. The swirler and fuel nozzle are embedded to the entrance duct of the combustor. The body of the linear is considered corrugated with cylindrical 18 serrations. The stainless-steel material with thickness 3 mm overall for the combustor is considered. The discharge nozzle outlet diameter is 20 cm.

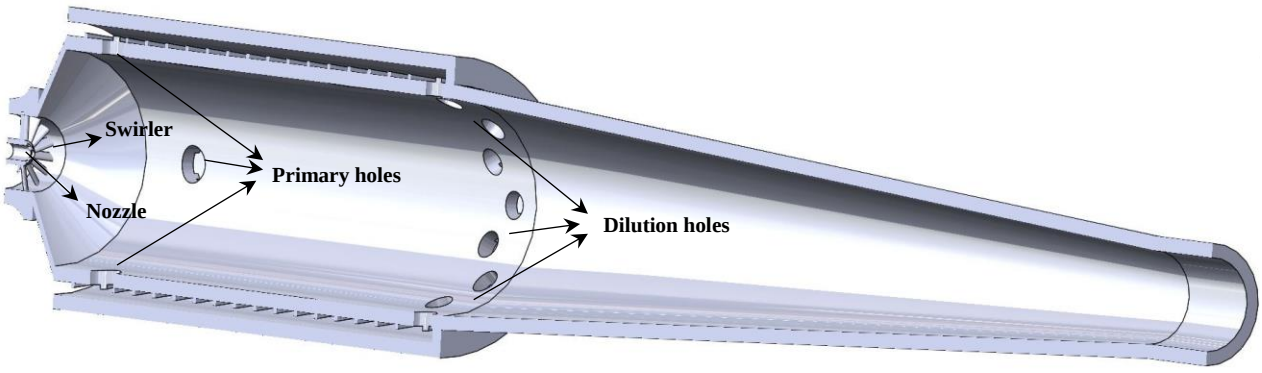

Fig 1 The schematic of the 3 kWe combustor for H_2/N_2

To calculate the fuel flow rate to power the turbine and combustor nozzle characteristics, the equilibrium combustion of H_2/N_2 was simulated and analyzed. Fig 2 gives the schematic of the Aspen Plus process simulation flow diagram for fuel flow rate calculations. The fuel flow rate was obtained

8.042 gr/sec and fuel required pressure is 190.8 kPa (Calculated from $\boldsymbol{P_{fuel} = P_{combustor} + 2\,\Delta P_{pressure\ drop}}$)

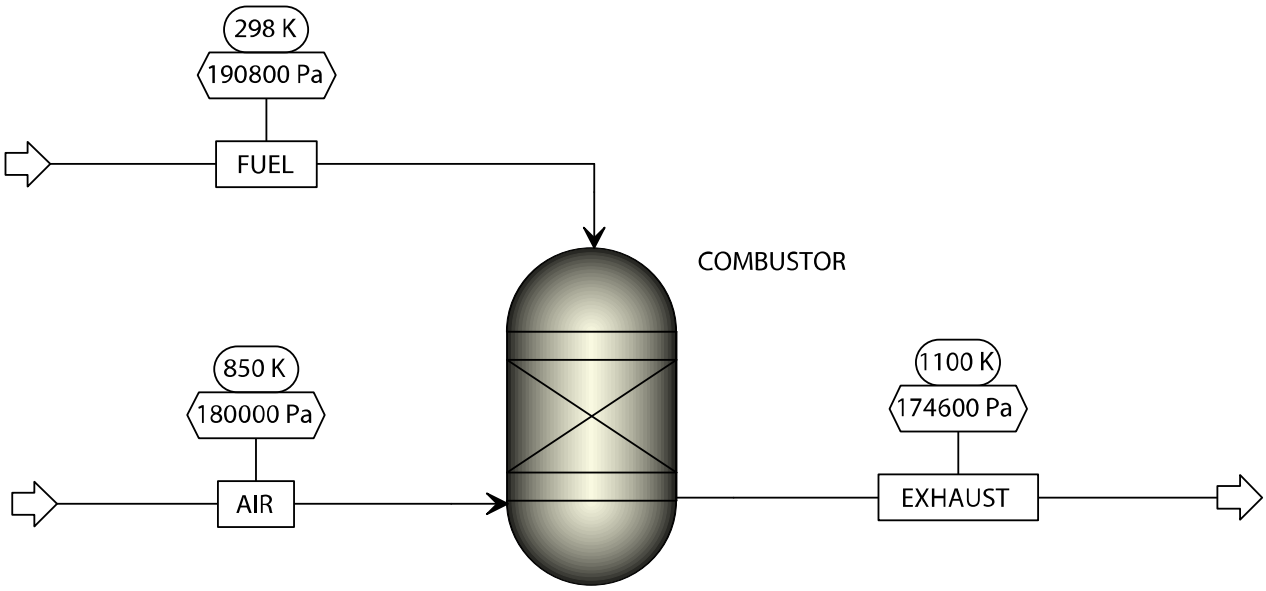

Fig 2 The Aspen Plus simulation flow diagram of the microturbine combustor

The fuel nozzle was designed based on the required fuel pressure and flow rate using Bernoulli equation. Nine fuel passage were considered for the nozzle, one along the combustor axis and eight with 45^o inclination angle. The fuel nozzle diameter was obtained 1.7 mm for the coaxial hole and 9.85 for the inclined holes.

An axial swirler inclined 40^o was considered and embedded into the duct of the combustor. The shape of the vanes and an area they allocate to the swirl air to enter the combustor were designed specifically based on the 3% combustor overall pressure drop and share of the air considered as the swirl air (in this case: 7%). The position of the swirl vanes and nozzle both in the combustor duct was achieved through the optimization stage to avoid any flashback and high thermal stress on the combustor walls. Four Primary holes with diameter 8 mm and sixteen dilution holes with diameter 6 were considered on the liner to stage the air within the combustor. The primary and dilution air holes were embedded in the liner at distances 35 and 200 mm from beginning of the combustor duct, respectively. The stainless-steel material is considered for the components of the combustor.

3. Model formulation

The modelling of the combustor was performed using ANSYS 19.2 Software to research the H_2/N_2 flame in the designed microturbine combustor. The conservation equations of mass, momentum and energy are achieved using a steady-state solver with no Dufour effects, no work by pressure and viscous forces, no surface reactions and no gas radiation.

$$\nabla.\left(\rho \vec{u}\right) = 0 \quad \textbf{(1)}$$

$$\rho\left(\vec{u}.\nabla\vec{u}\right) = -\nabla p + \nabla.\left[\mu\left(\nabla\vec{u} + \left(\nabla\vec{u}\right)^T - \frac{2}{3}\nabla.\vec{u}I\right)\right] \quad \textbf{(2)}$$

$$\nabla.\vec{u}\left(\rho E_f + p\right) = \nabla.\left[k_{eff}\nabla T - \sum_j h_j J_j + \left(\mu\left(\nabla\vec{u} + \left(\nabla\vec{u}\right)^T - \frac{2}{3}\nabla.\vec{u}I\right)\vec{u}\right)\right] + S_f^h \quad \textbf{(3)}$$

where ρ, $\vec{u}$, p, μ, I, T, E_f, k_{eff}, $\vec{J}_j$, h_j, and S_f^h denote gas density, velocity vector, absolute pressure, molecular viscosity, unit tensor, temperature, total fluid energy, effective conductivity, diffusion flux of species j, enthalpy of species j, and fluid enthalpy source term, respectively. For the combustor walls, the conservation of energy is maintained:

$$\nabla.\left(k_w.\nabla T\right) = 0 \quad \textbf{(4)}$$

where k_w is the thermal conductivity of the wall.

To model the combustion, the conservation of species is required:

$$\nabla\left(\rho\vec{u}Y_j\right) = -\nabla\vec{J}_j + R_j \quad \textbf{(5)}$$

In this equation, Y_j and R_j denote the mass fraction and the net production rate of the species in chemical reactions.

A transport equation for entropy is also solved:

$$Tds = du + pd\left(1/\rho\right) - \sum_{j=1}^{n} m_j d\left(n_j/\rho\right) \quad \textbf{(6)}$$

where s indicates the specific entropy, u denotes the specific internal entergy, m_j represents the chemical potential of species j, and n_j is the number density of specie j. The entropy generation S_{gen} in the combustor is defined as follows:

$$S_{gen} = \dot{m}s \quad \textbf{(7)}$$

where $\dot{m}$ is the flow rate of gas.

The exergy destructuve E_{des} in the combustor is germane to the overall entropy generation as follows:

$$E_{des} = S_{gen}T_0 \quad \textbf{(8)}$$

T_0 represents the ambient temperature, 850 K.

According to second law of thermodynamics, the exergy efficiency is defined as follows:

$$h_{\Ö} = \left(1 - \frac{E_{des} + E_{loss}}{\dot{m}_{H_2} Q_{LHV}}\right) 100\% \quad \textbf{(9)}$$

In this equation, E_{loss} represents the energy exiting the combustor by the flue gas, $\dot{m}_{H_2}$ and Q_{LHV} denote the mass flow rate and lower heating value of hydrogen, 119.96 MJ/kg.

The above-mentioned equations are solved in the combustion computational domain using appropriate following modelling consideration. The shear stress transport turbulence model is considered to the model the highly reactive turbulence flows in the combustor [28]. The flamelet concept with 32 diffusion flames in 64 grid points was utilized to model the chemistry of the flame. For this case, a Li hydrogen combustion mechanism [29] is considered with 13 extra reaction among nitrogen oxides. Fig 3 gives the path-line of reaction among nitrogen oxides considered to conduct this simulation.

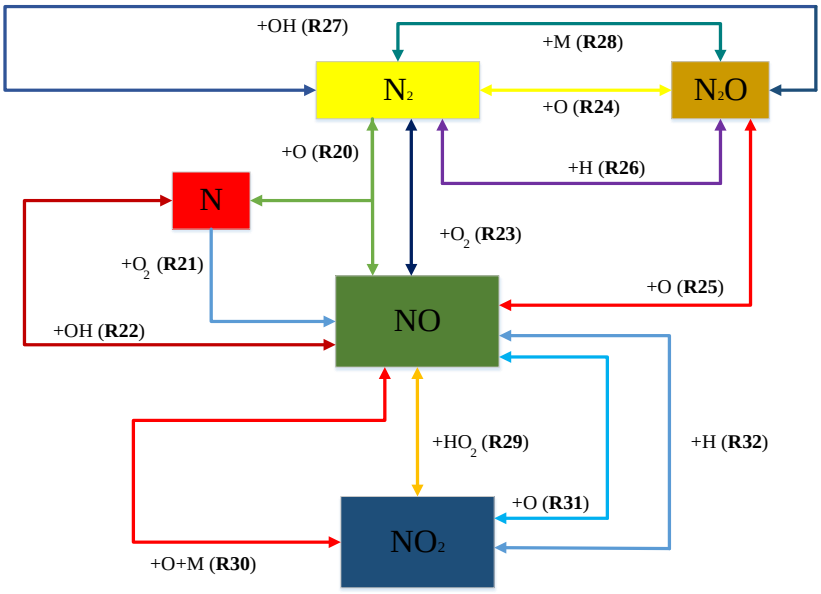

Fig 3 The path-line of reaction among nitrogen oxides

Table 1 $N_2/H_2/O_2$ combustion mechanism, $k = AT^n \exp(-E/RT)$.

NO	Reaction		A (cm, mol, s)	n	E (kcal mol^{-1})
(R1)	$H + O_2 \; f \;\; O + OH$		3.55×10^{15}	-0.41	16.6
(R2)	$O + H_2 \; f \;\; OH + H$		5.08×10^{04}	2.67	6.29
(R3)	$H_2 + OH \; f \;\; H_2O + H$		2.16×10^{08}	1.51	3.43
(R4)	$O + H_2O \; f \;\; OH + OH$		2.97×10^{06}	2.02	13.4
(R5)	$H_2 + M \; f \;\; H + H + M$		4.58×10^{19}	-1.40	104.38
(R6)	$O + O + M \; f \;\; O_2 + M^a$		6.16×10^{15}	-0.500	0.00
(R7)	$O + H + M \; f \;\; OH + M^a$		4.71×10^{18}	-1.00	0.00
(R8)	$H + OH + M \; f \;\; H_2O + M^a$		3.80×10^{22}	-2.00	0.00
(R9)	$H + O_2 + M \; f \;\; HO_2 + M^b$	k_0	6.37×10^{20}	-1.72	0.52
		k_∞	1.48×10^{12}	0.60	0.00
(R10)	$HO_2 + H \; f \;\; H_2 + O_2$		1.66×10^{13}	0.00	0.82
(R11)	$HO_2 + H \; f \;\; OH + OH$		7.08×10^{13}	0.00	0.30
(R12)	$HO_2 + O \; f \;\; OH + O_2$		3.25×10^{13}	0.00	0.00
(R13)	$HO_2 + OH \; f \;\; H_2O + O_2$		2.89×10^{13}	0.00	-0.50
(R14)	$HO_2 + HO_2 \; f \;\; H_2O_2 + O_2^c$		4.20×10^{14}	0.00	11.98
	$HO_2 + HO_2 \; f \;\; H_2O_2 + O_2$		1.30×10^{11}	0.00	-1.63
(R15)	$H_2O_2 + M \; f \;\; 2OH + M^d$	k_0	1.20×10^{17}	0.00	45.5
		k_∞	2.95×10^{14}	0.00	48.4
(R16)	$H_2O_2 + H \; f \;\; H_2O + OH$		2.41×10^{13}	0.00	3.97
(R17)	$H_2O_2 + H \; f \;\; HO_2 + H_2$		4.82×10^{13}	0.00	7.95

(R18)	$H_2O_2 + O \; f \;\; OH + HO_2$	9.55×10^{06}	2.00	3.97
(R19)	$H_2O_2 + OH \; f \;\; HO_2 + H_2O^c$	1.00×10^{12}	0.00	0.00
	$H_2O_2 + OH \; f \;\; HO_2 + H_2O$	5.80×10^{14}	0.00	9.56
(R20)	$N + NO \; f \;\; N_2 + O$	3.50×10^{13}	0.00	0.33
(R21)	$N + O_2 \; f \;\; NO + O$	2.65×10^{12}	0.00	6.40
(R22)	$N + OH \; f \;\; NO + H$	7.333×10^{13}	0.00	1.12
(R23)	$NO + NO \; f \;\; N_2 + O_2$	3.00×10^{11}	0.00	65.0
(R24)	$N_2O + O \; f \;\; N_2 + O_2$	1.40×10^{12}	0.00	10.810
(R25)	$N_2O + O \; f \;\; NO + NO$	2.90×10^{13}	0.00	23.15
(R26)	$N_2O + H \; f \;\; N_2 + OH$	4.40×10^{14}	0.00	18.88
(R27)	$N_2O + OH \; f \;\; N_2 + HO_2$	2.00×10^{12}	0.00	21.06
(R28)	$N_2O + M \; f \;\; N_2 + O + M$	1.30×10^{11}	0.00	59.62
(R29)	$NO + HO_2 \; f \;\; NO_2 + OH$	2.11×10^{12}	0.00	-0.48
(R30)	$NO + O + M \; f \;\; NO_2 + M$	1.06×10^{20}	-1.41	0.00
(R31)	$NO_2 + O \; f \;\; NO + O_2$	3.90×10^{12}	0.00	-0.24
(R32)	$NO_2 + H \; f \;\; NO + OH$	1.32×10^{14}	0.00	0.360

[a] Efficiency factor for $\varepsilon_{H_2O} = 12$ and $\varepsilon_{H_2} = 12$.

[b] Troe parameter is F_c=0.8. Efficiency factor for $\varepsilon_{H_2O} = 12$. Efficiency factor for $\varepsilon_{H_2O} = 11$, $\varepsilon_{H_2} = 2$ and $\varepsilon_{O_2} = 0.78$.

[c] (R14) and (R19) are expressed as the sum of the two rate expressions.

[d] Troe parameter is F_c=0.5. Efficiency factor for $\varepsilon_{H_2O} = 12$ and $\varepsilon_{H_2} = 2.5$.

The density and specific heat of the H_2/air are obtained by incompressible-ideal-gas law and mixing law, respectively. The gas mixture thermal conductivity and viscosity are calculated as a mass fraction-weighted mean of all species, while the specific heat of species is extracted from a piecewise polynomial fitting of temperature.

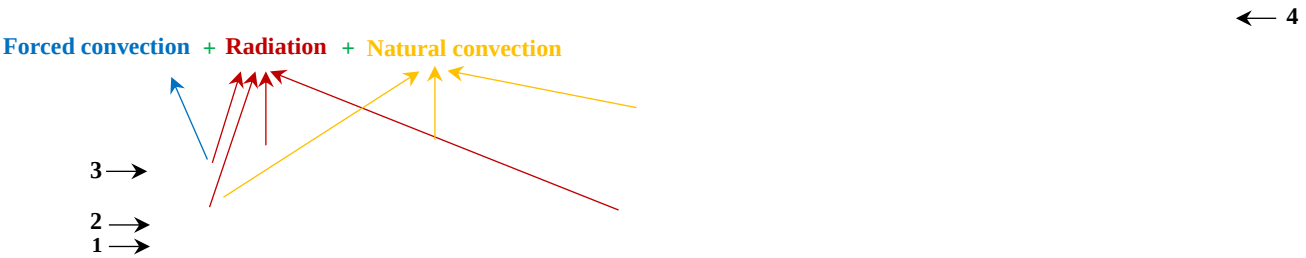

1- Fuel inlet **2- Swirl air inlet**

3- Staged air including primary and dilution **4- Outlet**

Fig 4 Computational domain

The computational domain and boundaries of the combustor is shown in Fig 4. The boundary conditions are set as: (1) three mass-flow-rate inlets are defined-one for fuel and two for swirl and staged air (including primary and dilution) to the liner are considered. The inlet pressure of the fuel and air were set as 190.8 and 180 kPa, respectively. The turbulent intensity for inlets are 5% and hydraulic diameters of the fuel, swirl and staged air inlets are 0.0034, 0.015, and 0.005 mm. The fuel mass fraction of species is $y_{H_2} = 0.02345$, $y_{O_2} = 0.0313$, $y_{H_2O} = 0.00126$, $y_{AR} = 0.01$, and $y_{N_2} = 0.96215$. (2) For combustor walls, zero diffusive flux for species and no slip condition for the entire fluid are employed at the gas-solid interfaces. For the liner wall, the radiation and turbulent hear transfer is considered, while for other walls the radiation in conjunction with natural convection heat transfer is employed. The heat transfer equation with the environment is obtained from the following:

$$Q_{loss} = h_0 \text{å}\ A_i\left(T_{w,i} - T_o\right) + es\ \text{å}\ A_i\left(T_{w,i}^4 - T_0^4\right) \quad \textbf{(10)}$$

where A_i denotes the surface area of grid cells, $T_{w,i}$ represents the temperature at the grid cells of the walls, s is the Stephan-Boltzman constant, $5.67' 10^{-8}\ W/\left(m^2K^4\right)$, h_0 denotes the heat transfer coefficient, 10 $W/\left(m^2K\right)$ for natural convection heat transfer and 32 $W/\left(m^2K\right)$ for turbulent convection heat transfer, and e indicates the wall emissivity, 0.85. (3) For outlet, pressure-outlet

boundary condition is employed. The outlet gauge pressure is 174.6 kPa. The hydraulic diameter and turbulent intensity of the outlet 0.02 mm and 5%, respectively.

In finite volume part of the computational domain, simple algorithm is employed to solve the pressure velocity coupling and discretize the equations. All the equations are discretized by second order upwind method: the convergence criterion for continuity, momentum, and species is 10^{-3} and for energy equation is as 10^{-6}. A monitor for area-averaged-mean-temperature is also considered at the combustor outlet as an assurance for completion of simulation. Before final post processing of the results, several fine to coarse meshes are tested starting with 524,546 to 5,890,285 cells. Our preliminary analysis has shown that the by increasing the number of grids more than 6 million, the variation in results is less than 5%. Consequently, the 5.8 million grids are considered optimum in obtaining the required accuracy and saving computational costs for this study.

4. Result and discussion

The results are categorized into parts. In the first part, the combustor performance is analyzed in terms of velocity field, temperature, combustion efficiency, pressure drop for hydrogen fuel. In the second part, the combustor exergy, NO_X and operation in a 3 kW recuperated microturbine power generator are compared for hydrogen and natural gas.

4.1 Part I: Combustor characteristics for H_2/N_2

In this part, the aerodynamic field of the combustor, the temperature in the combustor and at it solid parts, combustion efficiency and pressure drop at the combustor axis are evaluated from the CFD results.

4.1.1 Velocity field

The qualitative feature of the designed combustor is displayed by the velocity field of H_2/N_2 highly reactive turbulent flow. The ensemble average of streamlines in the mid-horizontal and vertical planes are shown in Fig 5 (a) and (b). The flow topologies of the H_2/N_2 reactive jet are particularly suitable for showing the preciseness and comprehensiveness of the design. The central core vortex mildly interacts with the previous impinging primary jets, which drives some part as backflow in the

primary region. As a result, a part of H_2/N_2 coming from the angled holes is pushed towards the walls, forming the secondary recirculation zone. These features are necessary for autoignition of the fuel in the combustor.

The primary port cross section (Fig 5 (c)) has shown that part of the air push back to the combustor walls leading to establishment of a secondary recirculation zone. This recirculation zone establishment near the primary holes curtails the flame impingement to the liner, as a result chilling the combustor walls. A similar radial backflow movement has also been observed at the dilution port cross section (Fig 5 (d)). The air jet penetration at the dilution port is also deep enough for the air to reach the center of combustor and cooling the fume.

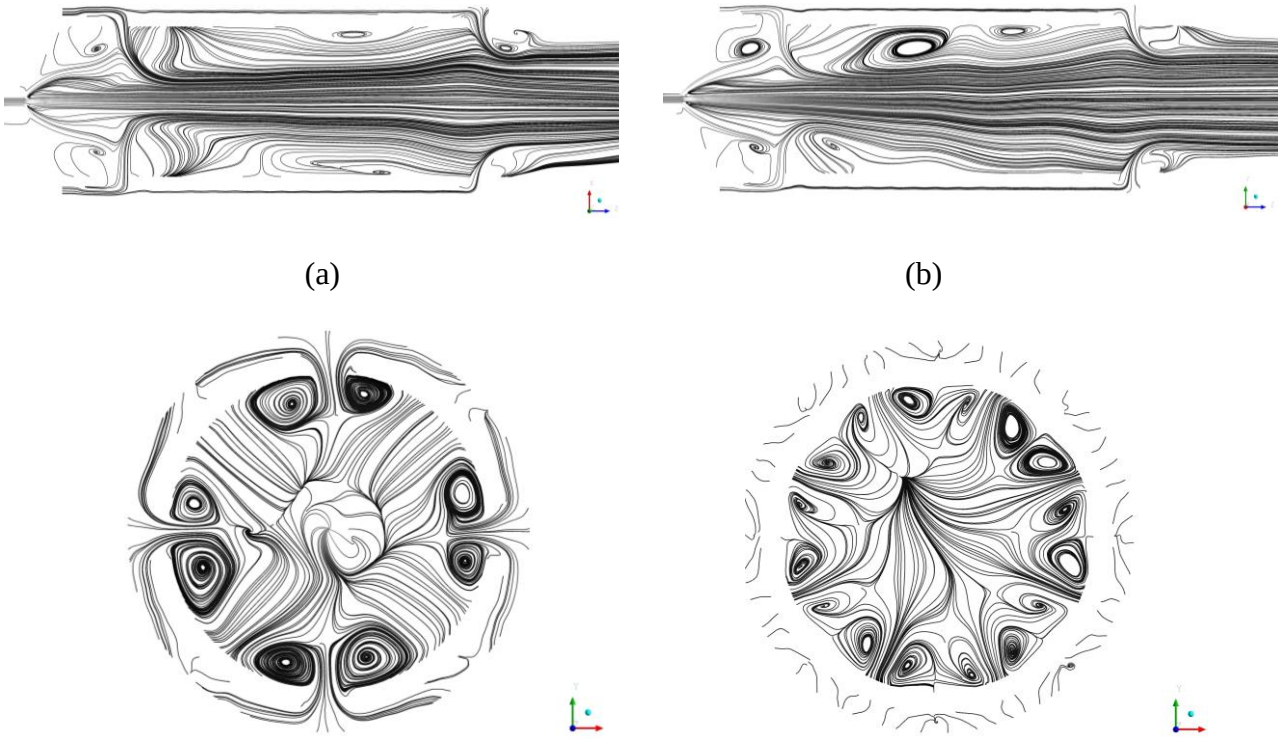

(a) (b)

(b) (d)

Fig 5 Reynolds averaged flow field, (a). Streamline in the vertical midplane Z-X. (b). Streamline in the vertical midplane Z-Y. (c). Primary port cross section. (d). Dilution port cross section.

The impingement region of primary air at the center of the combustor delineates the strength of the recirculation zone at the combustor head. However, the nature of flow at dilution jet is of different nature. The flow pattern downstream of the primary jets is not that much under the influence of design

consideration including geometry of fuel nozzle and swirl characteristics. The penetration jet to the combustor center at the dilution port is rather symmetrical. This is from the prefect circular shape of discharge nozzle of the combustor.

4.1.2 Temperature

The occurrence of the combustion in the designed combustor fully mimics the features of flameless burners without any flame front and significant NO_X emissions. This is because 1) the hydrogen fuel is mixed with nitrogen, an inert gas to control the combustion 2) the reactive fluid temperature does not transcend 1450 K, 3) the combustion takes place over a large volume of gas. In this section, we have shown the feature of the designed combustor. Fig 6 (a) gives the velocity vectors in mid vertical place of the combustor. The primary jet momentum is not high enough to penetrate the central cortex of the fluid. Instead, it moves coaxially with instead of agitating the fuel stream. This brings about the large volumetric combustion with low spatial temperatures (Fig 6 (a)). The primary jet also helps the swirl air by deviating the fuel stream that moves towards the combustor liner, as a result controls the temperature at the walls (Fig 6 (b)). The swirl intensity is high enough to carry the mixture of hydrogen/nitrogen forward without any flame flashback and to narrow down the flame without any impingement to the combustor head.

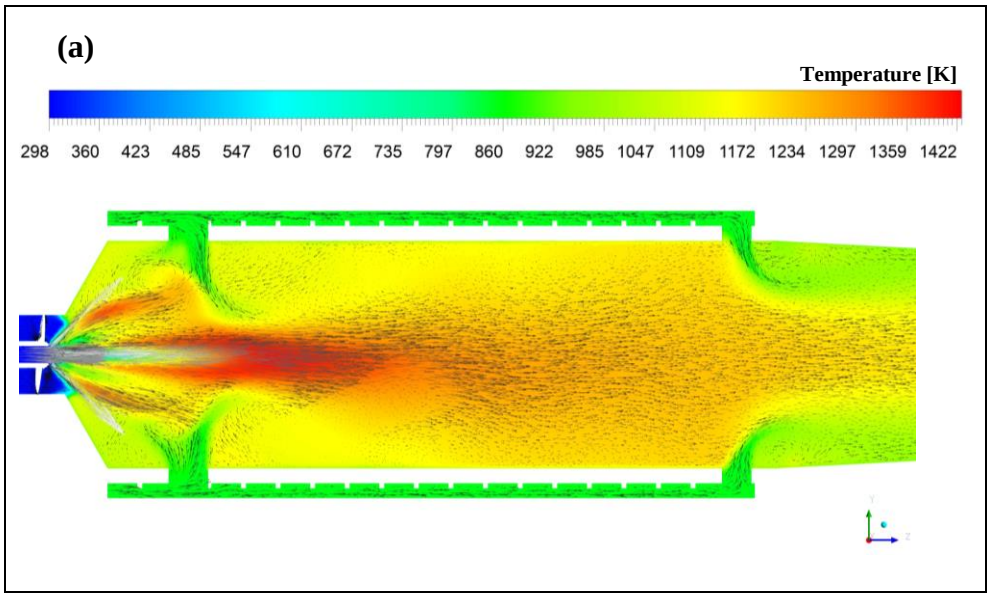

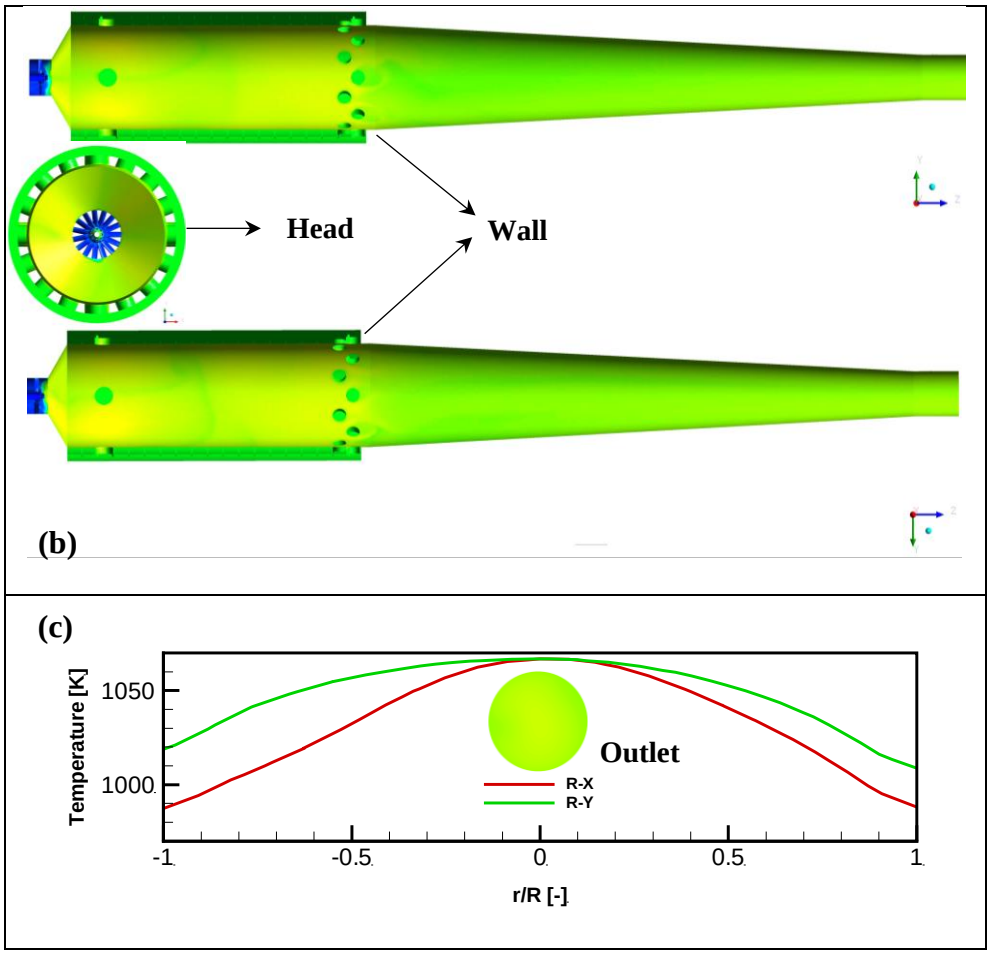

Fig 6 Reynolds averaged (a). Temperature and velocity vector in the vertical midplane Y-Z. (b). Wall Temperature. (c). Outlet temperature distribution.

The temperature profile (Fig 6 (a)) demonstrates that hot region is between the primary and dilution ports in the middle parts of the chamber. Indeed, no combustion occurs after the injection of dilution air and the flame is evidently stabilized in the head of the combustor and in the wake of the recirculation region. The liner wall is completely isolated from the fuel stream by primary jet and no fuel encroachment could be observed: no reaction approaches the liner wall which is evident from *green* layer in proximity of the wall in all the temperature profile. Also apparent is the high temperature of escaping fume from the primary region is fully controlled and went down in the discharge nozzle, leading to uniform outlet temperature distribution with a desired average value in design objectives (Fig 6 (c)). The effective control of temperature in the combustor leads to very low concentration of NO_X at the outlet plane.

4.1.3 Combustion efficiency

The combustion efficiency in percentage is reported here to show the capability of the combustor in completion of the combustion before the combustor outlet nozzle. Here, combustion efficiency is defined the heat loss from combustor outlet via the incomplete combustion products:

$$h = 1 - \frac{Q_{H_2}[H_2]}{Q_{H_2}[H_2]\not{c}} \, 100\%$$

where Q_{H_2} = 286 kJ/mol is hydrogen enthalpy of the combustion and $[H_2]$ is hydrogen spatial concentration in the combustor. The $[H_2]\not{c}$ denotes the average volumetric concentration of either the hydrogen in combustor when there is no combustion.

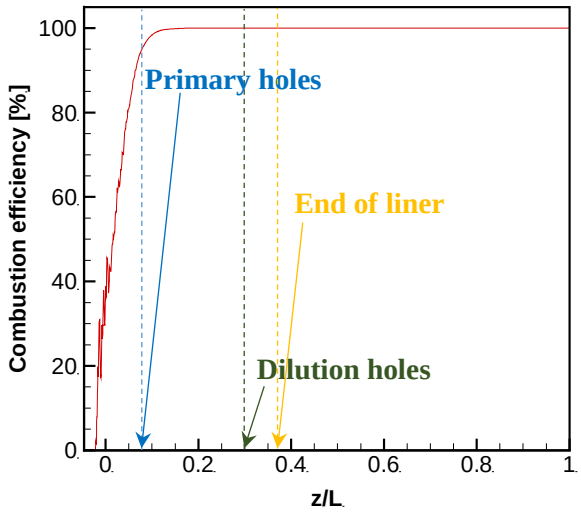

Fig 7 The spatial combustion efficiency at the axis of the combustor (z/L=0: end of liner head and beginning of the liner).

Fig 7 represents the value of combustion efficiency at the combustor axis. The length of the axis is normalized in this graph giving 0 for the beginning of the liner and 1 for the combustor outlet. The position of primary holes, and dilution holes at liner end surface are 0.07, 0.3, and 0.39, respectively. Fig 7 can show how the design can proceed the combustion to the completion. The combustion efficiency reaches almost 100% at 0.1 total combustor length. This length corresponds to a little distance further than primary holes and is well fallen before the dilution holes.

4.1.4 Pressure drop

The pressure drop is another key design parameter of the microturbine combustors. The fluid face acquire pressure drop because of change of in areas it passes through the primary, secondary and dilution holes and combustor outlet nozzle, if any. The influence of the combustor on the combustor pressure drop at the combustor axis is illustrated in Fig 8. It shows that how the microturbine fluid experiences pressure drop passing the combustor.

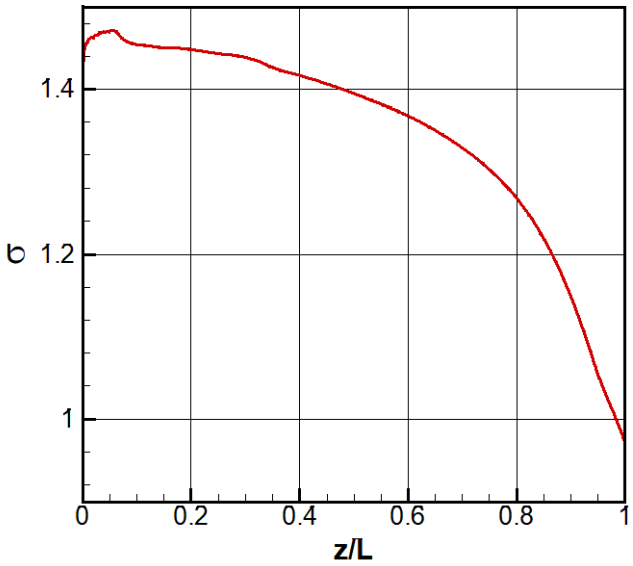

Fig 8 The pressure drop ratio at the axis

The s giving the proportion of the spatial pressures to the inlet air pressure $s = P/P_{inlet}$ is given in the Fig 8. The s is around 0.97 at the outlet giving the fluid pressure drop in the combustor around 3%. This meets the combustor design benchmarks and specification that was taken into account of considerations.

4.2 Comparison between hydrogen and methane

In this part, the NO_X and entropy, and finally the overall operation of the combustor for 3 kW energy power generation are evaluated, analyzed and compared for H_2 and natural gas. The natural gas is considered 94% methane, 0.04 ethane, 0.003 propane, 0.002 butane, 0.01 nitrogen, and 0.05 carbon dioxide (by mole). For Natural gas, the same strategy represented in section 2 is repeated to obtain the required natural gas flow rate to generate the 3 kW power. Then, the results for hydrogen and natural gas are analyzed in the following.

4.2.1 NO_X

Thermal NO_X is main gaseous pollutant during the hydrogen combustion as the hydrogen combustion leads to a very high temperature and no carbon exists in the fuel. The formation of NO_2 is also simulated as the temperature in the combustor does not surpass 1500 K, as a result the level of nitrogen dioxide is on the par of nitrogen monoxide [30]. NO_X is deemed the mixture including NO, NO_2, and N_2O for this analysis. The level of NO_X emission here is reported for dry gas based on 15% oxygen content.

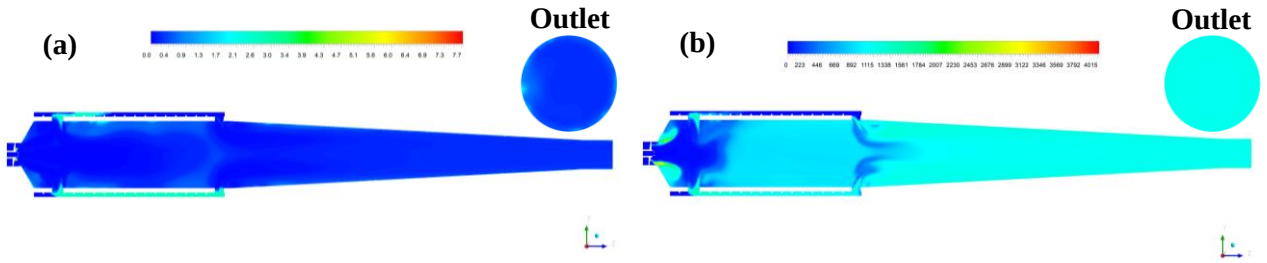

Fig 9 Contour plots of NO_X [mgr/m^3]; a) Flameless hydrogen combustion, b) Natural gas.

The contour plot of NO_X emission is given in Fig 9 at the plane ZY and combustor outlet. Fig 9 (a) has shown that the design for N_2/H_2 could successfully meet the expectations, providing a flameless-NO_X less combustion. It shows that for hydrogen the level of NO_X does not transcend the 1 ppb of the combustion mixture. At the combustor outlet, the NO_X is 0.4 ppb (mgr/m^3) for hydrogen. However, NO_X for natural gas was achieved 1143 ppb for natural gas. Comparing the Fig 9 (a) and (b) shows that level of NO_X during natural gas combustion is comparatively higher with significant orders of magnitude 10^{+3} than hydrogen combustion.

4.2.2 Entropy

The entropy destruction for both hydrogen and natural gas fuels are compared in the designed 3 kW microturbine combustor. The contour plots of Fig 10 shows variation of entropy. For this combustor, the entropy variation is very much consistent with temperature variations. The entropy at the combustor outlet for hydrogen and natural gas were 8395 and 8383 $J/kg.K$, respectively.

(a) **(b)**

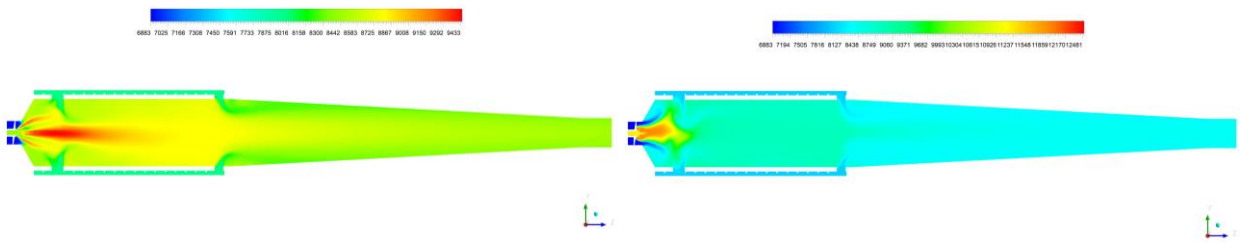

Fig 10 Contour plots of Entropy [$J/kg.K$]; a) Flameless hydrogen combustion, b) Natural gas.

Comparing it for hydrogen and natural gas, it can be readily seen that the entropy generation as well as destruction for natural gas is higher than hydrogen. The maximum entropy generation for natural gas is (12509 $J/kg.K$), while for hydrogen flameless combustion is (9446.19 $J/kg.K$). As a result, the entropy destruction of natural gas is 4126 $J/kg.K$, while for hydrogen fuel it is only 1051 $J/kg.K$. This less entropy destruction in H_2/N_2 combustion indeed leads to more exergy loss from the combustor when the hydrogen ignites in the MT combustor.

4.2.3 Combustor in power generation

The overall performance of the designed combustor for hydrogen fuel is analyzed here in a process plant as shown in Fig 11. When the output power of the turbine is kept constant, the choice of the fuel could influence the recuperator effectiveness (ε), and thermal efficiency ($h_{th,regen}$):

$$e = \frac{q_{regen,act}}{q_{regen,\max}} \quad \textbf{(11)}$$

$$h_{th,regen} = \frac{w_{turb} + w_{comp}}{q_H} \quad \textbf{(12)}$$

The recuperator effectiveness is a ratio showing the real to maximum amount of heat that could be transferred from the recuperator. For two different fuels, it depends on the thermal and chemical specifications of exhaust gas from the microturbine. The cycle overall efficiency represents the effective ratio of energy conversion in the microturbine overall.

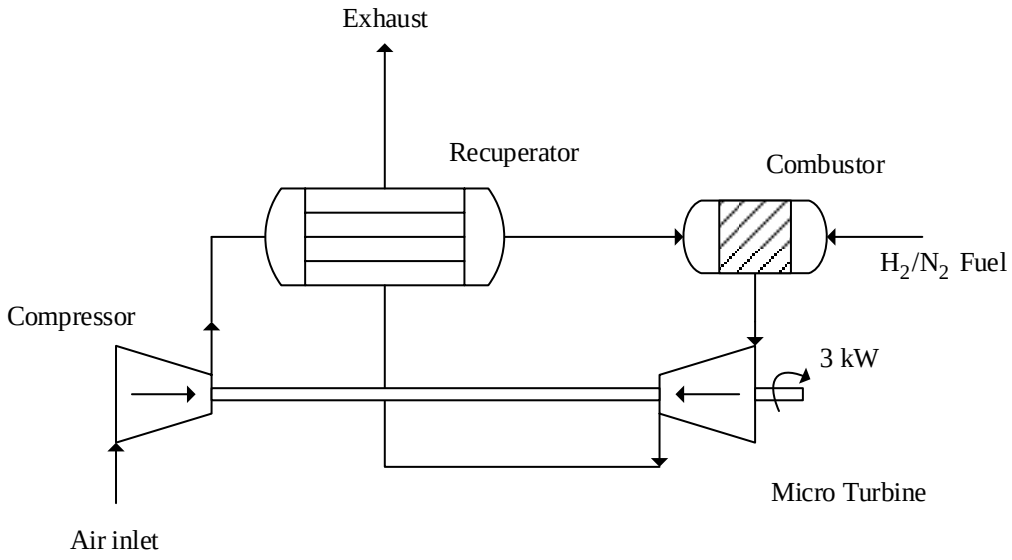

Fig 11. Recuperated 3 kW microturbine cycle with the designed combustor

The T-S diagram of the ideal recuperated Bryton cycle with the new combustor is also given Fig 12. From the graph, the values of the recuperator effectiveness is achieved 0.74 for hydrogen and 0.76 for natural gas. This slight difference among the recuperator effectiveness, however, is not because of different potency of the fuels exhaust in heating transfer. In return, it is achieved because of the different temperatures of microturbine exhaust and exhaust form the cycle overall. This different temperature is observed mainly because of the combustor which emanates hot gas with different components. The different species in the combustor flue gas has different thermal specifications (C_p) that obtain different temperature when they lose a constant heat in the recuperator. The recuperator duty is to provide heat and increase the temperature of the compressed air from standard conditions to 850 K.

The cycle efficiency for hydrogen and natural gas were 29% and 26%, respectively. The difference among the cycle efficiency was obtained mainly because of the release of energy in the combustor. The fact that hydrogen heating density is more than NG gives rise to the higher overall efficiency of microturbine with hydrogen fuel compared to NG.

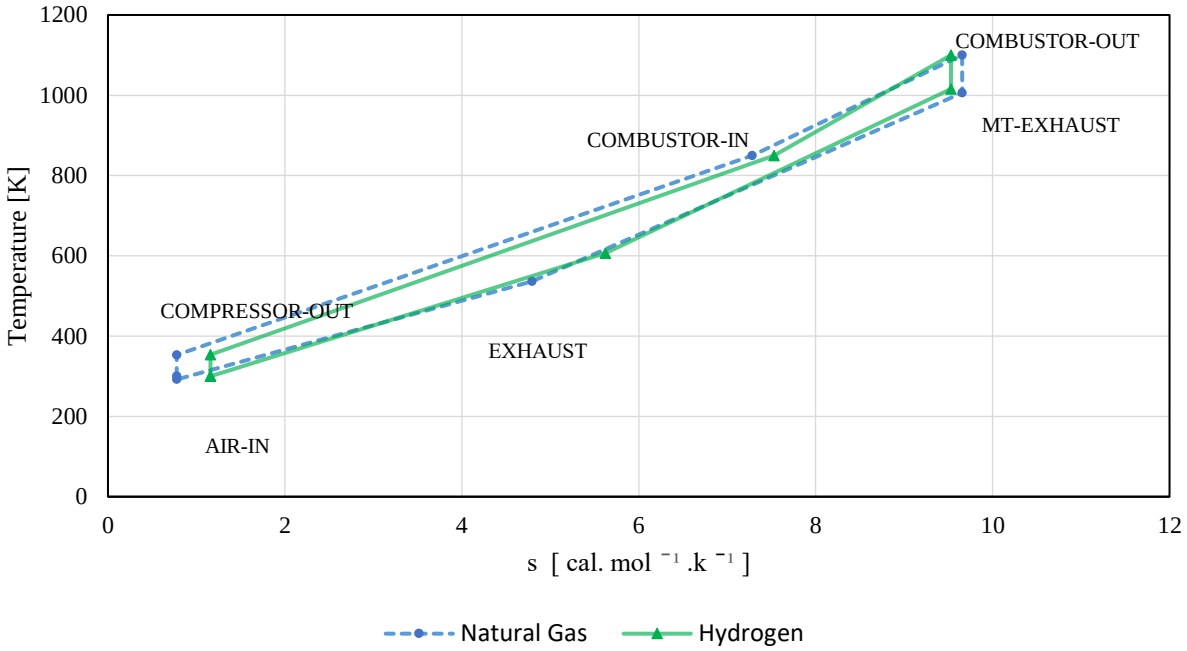

Fig 12. T-S diagram of the combustor with H_2 and natural gas

5. Conclusion

A new flameless combustor for hydrogen fuel is designed and optimized in the presented work to provide 3 kW energy. The aerodynamic of the combustor and temperature profiles of the combustor is analyzed to show the establishment of recirculation zones and swirl intensity and how this helps forming a flameless combustion. Afterwards, the design considerations in the pressure drop and combustion efficiency of the hydrogen flame is discussed and commented. Finally, the operation of the combustor in terms of NO_X and entropy generation, and the entire microturbine cycle is analyzed and compared for hydrogen and natural gas. Through the design procedure and comparison, the following conclusions are achieved:

1) To achieve flameless combustion, the air should move coaxially along the fuel jet so that the combustion occurs volumetric without flame front and significant rise of spatial temperatures. At this state, the combustor mimics the condition of a diffusion flame. For this purpose, two serios of holes are considered in the body of the liner: 1) primary holes, and dilution holes. The primary holes are key components in the design criteria. They are designed in the vicinity of the combustor head to both control the temperature of head as well as liner walls. The air

distribution is another key parametric design consideration in the aerodynamic of the combustor leading to large volumetric combustion of hydrogen and combustion stability between the primary and dilution holes. For this combustor, the air distribution is 15% by mass for swirl 23% for primary and 62% for dilution holes

2) In this flameless combustor, the amount of swirl air is not enough to carry the fuel mixture and stabilized the flame kernel reaction zone well in front of the fuel nozzle. As a result, an amount of pressurized fuel moves backward first because they encounter low pressure from the incoming swirl air. The position of nozzle was obtained in the optimization state to avoid any flame flashback that may be resulted from dilution of hydrogen with nitrogen.
3) The entropy analysis and NO_X emission of the combustor reveals that the entropy destruction and NO_X emission for hydrogen flame is remarkably lower than the natural gas. The NO_X for hydrogen at the combustor outlet plane was 0.4 mgr/m^3 . The entropy destruction for hydrogen flame is 3075 $J/kg.K$ lower than natural gas leading to lower exergy loss and higher energy efficiency for the flameless hydrogen combustion.
4) The operation of the combustor in the microturbine cycle is also analyzed and compared for natural gas and hydrogen. The T-S diagram of the cycle for both fuels reveals that cycle efficiency for hydrogen is 3% higher than natural gas, while the recuperator effectiveness is 0.02 lower.
5) Finally, it can be concluded that the air distribution, orientation of nozzle, its position, and the diameters of primary and secondary holes are all important in establishment of the flameless combustion in the combustor for hydrogen. These design considerations should be optimized for whatever the design is to achieve the better the advantages of renewable fuels.

Literature Cited:

[1] Ilbas M, Yılmaz İ, Kaplan Y. Investigations of hydrogen and hydrogen–hydrocarbon composite fuel combustion and NOx emission characteristics in a model combustor. International Journal of Hydrogen Energy. 2005;30(10):1139-47.
[2] Carcassi M, Fineschi F. Deflagrations of H 2–air and CH 4–air lean mixtures in a vented multi-compartment environment. Energy. 2005;30(8):1439-51.

[3] Choudhuri AR, Gollahalli SR. Characteristics of hydrogen–hydrocarbon composite fuel turbulent jet flames. International Journal of Hydrogen Energy. 2003;28(4):445-54.
[4] Karim GA. Hydrogen as a spark ignition engine fuel. International Journal of Hydrogen Energy. 2003;28(5):569-77.
[5] Jones JC. Energy-return-on-energy-invested for hydrogen fuel from the steam reforming of natural gas. Fuel. 2015;143:631.
[6] Maruta K. Micro and mesoscale combustion. Proceedings of the Combustion Institute. 2011;33(1):125-50.
[7] Ju Y, Maruta K. Microscale combustion: technology development and fundamental research. Progress in energy and combustion science. 2011;37(6):669-715.
[8] Bazooyar B, Ghorbani A, Shariati A. Combustion performance and emissions of petrodiesel and biodiesels based on various vegetable oils in a semi industrial boiler. Fuel. 2011;90(10):3078-92.
[9] Bazooyar B, Hallajbashi N, Shariati A, Ghorbani A. An investigation of the effect of input air upon combustion performance and emissions of biodiesel and diesel fuel in an experimental boiler. Energy Sources, Part A: Recovery, Utilization, and Environmental Effects. 2014;36(4):383-92.
[10] Bazooyar B, Hosseini SY, Moradi Ghoje Begloo S, Shariati A, Hashemabadi SH, Shaahmadi F. Mixed modified Fe2O3-WO3 as new fuel borne catalyst (FBC) for biodiesel fuel. Energy. 2018;149:438-53.
[11] Bazooyar B, Jomekian A, Shariati A. Analysis of the formation and interaction of nitrogen oxides in a rapeseed methyl ester nonpremixed turbulent flame. Energy & Fuels. 2017;31(8):8708-21.
[12] Bazooyar B, Shariati A. A comparison of the emission and thermal capacity of methyl ester of corn oil with diesel in an experimental boiler. Energy Sources, Part A: Recovery, Utilization, and Environmental Effects. 2013;35(17):1618-28.
[13] Bazooyar B, Shariati A, Hashemabadi SH. Economy of a utility boiler power plant fueled with vegetable oil, biodiesel, petrodiesel and their prevalent blends. Sustainable Production and Consumption. 2015;3:1-7.
[14] Ghorbani A, Bazooyar B. Optimization of the combustion of SOME (soybean oil methyl ester), B5, B10, B20 and petrodiesel in a semi industrial boiler. Energy. 2012;44(1):217-27.
[15] Ghorbani A, Bazooyar B, Shariati A, Jokar SM, Ajami H, Naderi A. A comparative study of combustion performance and emission of biodiesel blends and diesel in an experimental boiler. Applied Energy. 2011;88(12):4725-32.
[16] Bazooyar B, Hashemabadi SH, Shariati A. NOX formation of biodiesel in utility power plant boilers; Part B. Comparison of NO between biodiesel and petrodiesel. Fuel. 2016;182:323-32.
[17] Bazooyar B, Shariati A, Hashemabadi SH. Characterization and Reduction of NO during the Combustion of Biodiesel in a Semi-industrial Boiler. Energy & Fuels. 2015;29(10):6804-14.
[18] Gordon RL, Masri AR, Mastorakos E. Simultaneous Rayleigh temperature, OH-and CH 2 O-LIF imaging of methane jets in a vitiated coflow. Combustion and Flame. 2008;155(1):181-95.
[19] Luo K, Wang H, Yi F, Fan J. Direct numerical simulation study of an experimental lifted H2/N2 flame. Part 1: validation and flame structure. Energy & Fuels. 2012;26(10):6118-27.
[20] Michel J-B, Colin O, Angelberger C, Veynante D. Using the tabulated diffusion flamelet model ADF-PCM to simulate a lifted methane–air jet flame. Combustion and Flame. 2009;156(7):1318-31.
[21] Mouangue R, Obounou M, Mura A. Turbulent lifted flames of H 2/N 2 fuel issuing into a vitiated coflow investigated using Lagrangian Intermittent Modelling. International Journal of Hydrogen Energy. 2014;39(24):13002-13.
[22] Patwardhan S, De S, Lakshmisha K, Raghunandan B. CMC simulations of lifted turbulent jet flame in a vitiated coflow. Proceedings of the Combustion Institute. 2009;32(2):1705-12.
[23] Wang H, Luo K, Yi F, Fan J. Direct numerical simulation study of an experimental lifted H2/N2 flame. Part 2: flame stabilization. Energy & Fuels. 2012;26(8):4830-9.
[24] Wang Z, Fan J, Zhou J, Cen K. Direct numerical simulation of hydrogen turbulent lifted jet flame in a vitiated coflow. Chinese Science Bulletin. 2007;52(15):2147-56.

[25] Wang Z, Zhou J, Cen K. Visualization of nonpremixed hydrogen jet flame in a vitiated coflow by DNS. Journal of Visualization. 2007;10(2):136-.
[26] Wu Z, Masri AR, Bilger RW. An experimental investigation of the turbulence structure of a lifted H2/N2 jet flame in a vitiated co-flow. Flow, turbulence and combustion. 2006;76(1):61-81.
[27] Lefebvre AH. Gas turbine combustion: CRC press, 1998.
[28] Menter FR. Two-equation eddy-viscosity turbulence models for engineering applications. AIAA journal. 1994;32(8):1598-605.
[29] Li J, Zhao Z, Kazakov A, Dryer FL. An updated comprehensive kinetic model of hydrogen combustion. International journal of chemical kinetics. 2004;36(10):566-75.
[30] Bazooyar B, Ebrahimzadeh E, Jomekian A, Shariati A. NOx Formation of Biodiesel in Utility Power Plant Boilers. Part A: Influence of Fuel Characteristics. Energy & Fuels. 2014;28(6):3778-92.